Supporting Information

Mn doping regulating electronic structure of Co_3O_4 to construct dual active sites for Oxygen electrocatalysis

Ziyi Shui [a], Huiying Tian [c], Hang Mu [d], Liuyun Xu [a], Xiaoming Gao [a]*, Xi Chen [b]**

[a] *College of Chemistry & Chemical Engineering, Yan'an University, Yan'an 716009, China*

[b] *School of Interdisciplinary Studies, Lingnan University, Hong Kong, China*

[c] *School of Chemistry and Chemical Engineering, Jining Normal University, Ulanqab 012000, China*

[d] *Northwest Rubber & Plastics Research & Design Institute Co.,Ltd. Xian yang, 712023, China*

Corresponding Author

*E-mail: m18182696780@163.com (Z. S.); ydgaoxm@126.com (X. G.); xichen863@hotmail.com (X. C.).

Experimental Methods

1. Materials syntheses

The $MnCo_2O_4$ catalyst was synthesized by a hydrothermal method. In a typical procedure, 0.289 g of $Co(NO_3)_2 \cdot 6H_2O$ and 0.125 g of $Mn(NO_3)_2 \cdot 4H_2O$ were dissolved in 50 mL of deionized water with vigorous stirring to form a transparent solution. Subsequently, 50 mL of NaOH solution was introduced into the mixture. After stirring for 1 hour, the resulting precipitate was collected by centrifugation, washed several times with ethanol and deionized water, and then dried overnight. he dried products were ground into a fine powder and calcined at 500 °C in air for 3 hours to obtain $MnCo_2O_4$ nanoparticles. For comparison, pristine Co_3O_4 was synthesized using the same procedure, excluding the addition of $Mn(NO_3)_2 \cdot 4H_2O$.

2. Materials characterization

The crystal structure and phase composition of the samples were qualitatively analyzed by powder X-ray diffraction (Rigaku Ultima IV). X-ray photoelectron spectroscopy (XPS, Thermo Scientific ESCALAB Xi+) was was conducted to investigate the surface chemical composition, with Al Kα X-rays as the excitation source. The morphology and structure were observed by scanning electron microscopy (SEM, JEOL (JSM-7610 F)) and transmission electron microscope (TEM, JEOLF200). The surface areas of the samples were examined by the Brunauer-Emmett-Teller (BET) method with a Micromeritics ASAP 2450 instrument, while the pore size distributions were determined by the Barrett-Joyner-Halenda (BJH) method from the adsorption branches of the isotherms.

3. Electrochemical measurements

The electrochemical techniques of linear sweep voltammetry (LSV), Tafel plot (TAFEL), electrochemical impedance spectroscopy (EIS) and chronoamperometry (CA) were conducted using a CHI 760E electrochemical workstation with a rotating disk-ring electrode (RRDE) in 0.1 M KOH solution at room temperature (25℃). The typical three-electrode setup consisted of a glassy carbon working electrode, an Ag/AgCl reference electrode, and a graphite rod counter electrode. A catalyst mixture was prepared by sonicating 5 mg of catalyst, 5 mg of black carbon, 40 μL of Nafion, and 1 mL of ethanol for 1 hour to create a homogeneous ink. Subsequently, 5 μL of catalyst ink was deposited on the glassy carbon electrode (GC), with an area of 0.1965 cm^2. The polarization curves for ORR/OER were measured on the electrochemical workstation, with all potentials corrected to the reversible hydrogen electrode (RHE) and for IR drop.

4. Rechargeable zinc-air battery

To assess the practical application potential of the as-prepared catalysts, the catalyst inks was coated on commercial carbon cloths as air cathodes with a loading of 2 $mg \cdot cm^{-2}$. Zinc foil anode was dissolved in a solution of 6 M KOH and 0.2 M $Zn(Ac)_2$ to form zincate. The charge-discharge cycle performance of the battery was evaluated by LADN electricity, and the open-circuit voltage along with the charge-discharge polarization curves were measured by the CHI 760E electrochemical workstation.

5. Theoretical calculations

The energy barrier of Co_3O_4 and $MnCo_2O_4$ was performed using DFT with the Vienna ab initio simulation package (VASP) [1-2]. The Perdew-Burke-Ernzerhof (PBE) generalized gradient approximation (GGA) was applied for the exchange-correlation energy functional[3-4]. The projected augmented wave (PAW) pseudopotential depicted the ion core with periodic boundary conditions[5].

A 2 × 1 supercell consisting of three layers of Co_3O_4 (100) and $MnCo_2O_4$ (100) surfaces was constructed for the models. Geometry optimizations and free energy assessments were carried out with convergence thresholds of 10^{-6} eV for energy and 0.01 eV/Å for force. To address self-interaction errors due to strong correlation effects in 3d transition metal oxides, the Hubbard U parameter (GGA+U) was applied to Mn and Co with values of 3.96 eV and 3.4 eV, respectively [6-7]. A 15 Å vacuum in the z-direction minimized interactions between periodic images.

The free energy of ORR/OER was calculated by using the equation:

$$\Delta G = E_{surface + adsorbate} - E_{surface} - E_{adsorbate} + \Delta E_{ZPE} - T\Delta S \quad (1)$$

where G, E, ZPE and TS represent the free energy, total energy from DFT calculations, zero-point energy and entropic contributions, respectively.

Computational hydrogen electrode (CHE) model was used to study the thermodynamics of ORR and OER on catalysts. In CHE model, the free energy of ($H^+ + e^-$) equals to (1/2 H_2 (g)) for standard hydrogen electrode (SHE). For the four-electron pathway ORR in an alkaline electrolyte, the overall reaction is divided into four elementary steps:

(1) O_2 (g) + H_2O (l) + e^- + * = OOH* + OH^- (2)

(2) OOH* + e^- = O* + OH^- (3)

(3) O* + H_2O (l) + e^- = OH* + OH^- (4)

(4) OH*+ e^- = * + OH (5)

where the asterisk denotes a surface-bound species. For OER in an alkaline electrolyte, the overall reaction is the reverse reaction of ORR.

The Gibbs free energies of ORR and OER were calculated according to the method developed by Norskov and his co-workers[8-9].

$$U_{L,ORR} = 1.23 - \min\{\Delta G_{1-4}\}/e \quad (6)$$

$$U_{L,OER} = \max\{\Delta G_{1-4}\}e - 1.23 \quad (7)$$

For OER on both RuO_2 and MnO_2, either step (2) or step (3) is potential determining, while the limiting potential of ORR is raised from step (1) or step (4). Appling the linear scaling relation between ΔG_{OH} and ΔG_{OOH} ($\Delta G_{OOH} = \Delta G_{OH} + 3.2$).

$$U_{L,ORR} = 1.23 - \min\{\Delta G_{OH}, 4.92 - (3.2 + \Delta G_{OH})\}/e \quad (8)$$

$$U_{L,OER} = \max\{\Delta G_O - \Delta G_{OH}, 3.2 - (\Delta G_O - \Delta G_{OH})\}/e - 1.23 \quad (9)$$

The optimum ΔG_{OH} for ORR is derived as (4.92-3.2)/2=0.86 eV, and the optimum $\Delta G_O - \Delta G_{OH}$ for OER is thus set to 3.2/2=1.6 eV. Notably, the above derivation of optimal descriptor value is only for guiding the catalysts screening, the variation of the linear scaling relation will cause the deviation of the optimal descriptor value.

Supplementary Results

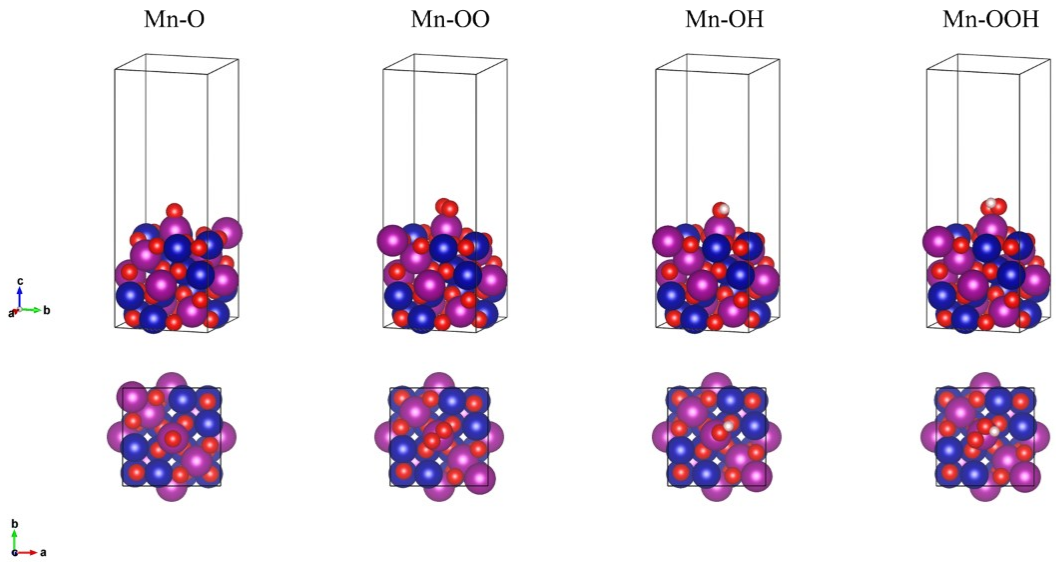

Fig. S1 The various adsorption intermediates on Mn site in the modes of $MnCo_2O_4$.

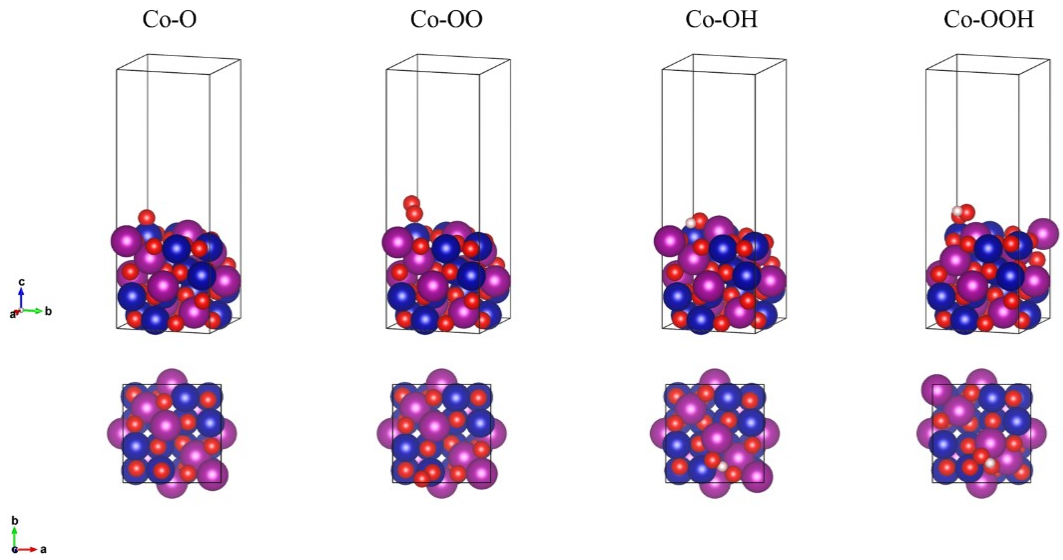

Fig. S2 The various adsorption intermediates on Mn site in the modes of $MnCo_2O_4$.

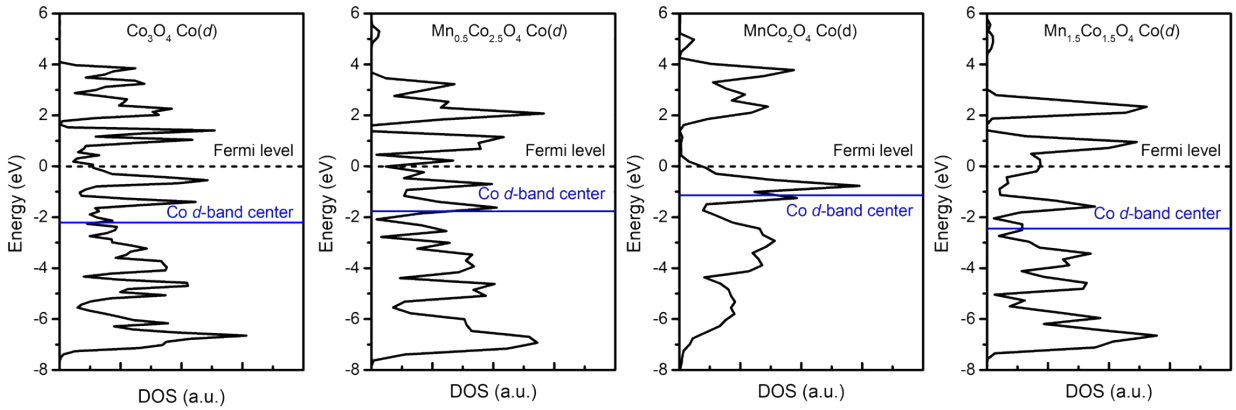

Fig. S3 Co d-band center relative to the Fermi surface of Co_3O_4, $Mn_{0.5}Co_{2.5}O_4$, $MnCo_2O_4$, and $Mn_{1.5}Co_{1.5}O_4$.

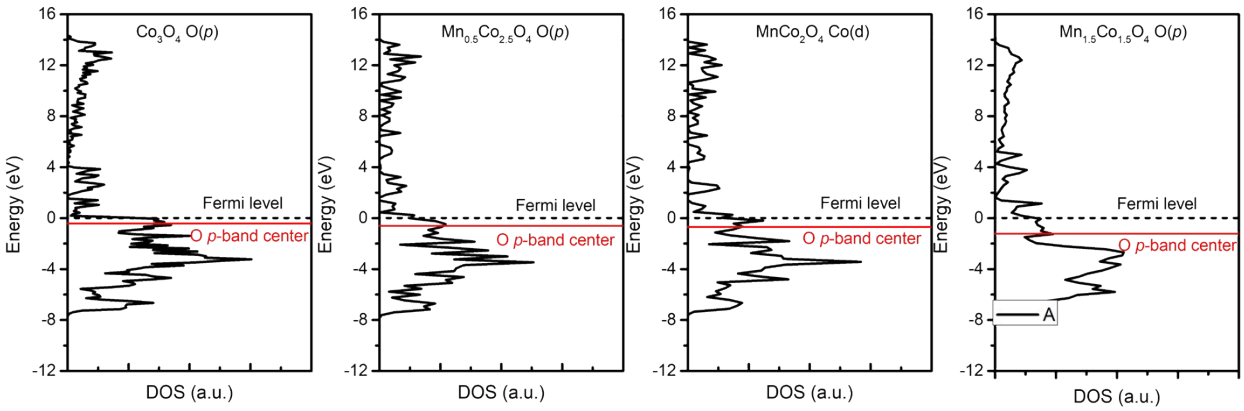

Fig. S4 O p-band centers relative to the Fermi surface of Co_3O_4, $Mn_{0.5}Co_{2.5}O_4$, $MnCo_2O_4$, and $Mn_{1.5}Co_{1.5}O_4$.

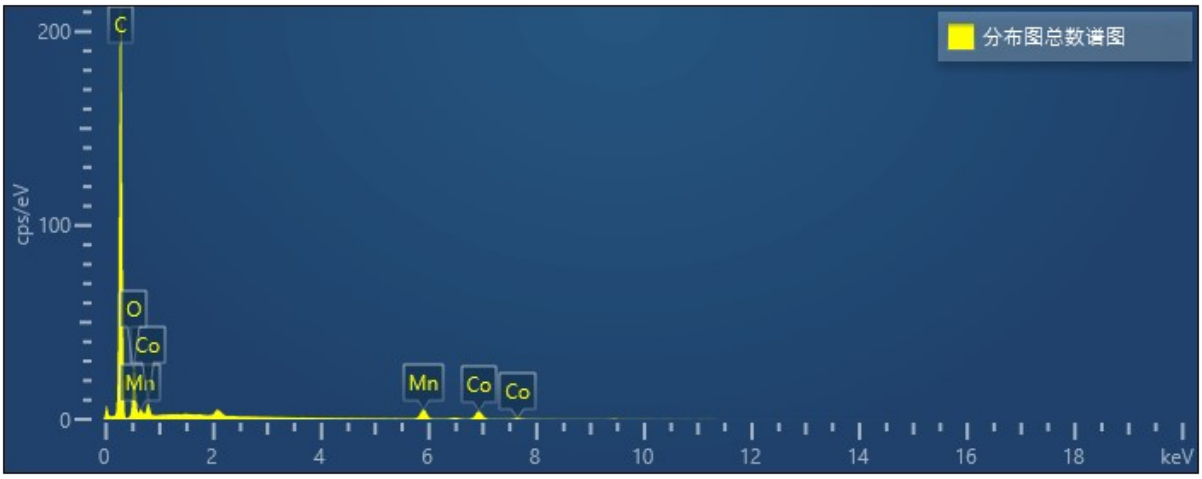

Fig. S5 EDS spectrum of $MnCo_2O_4$ catalyst.

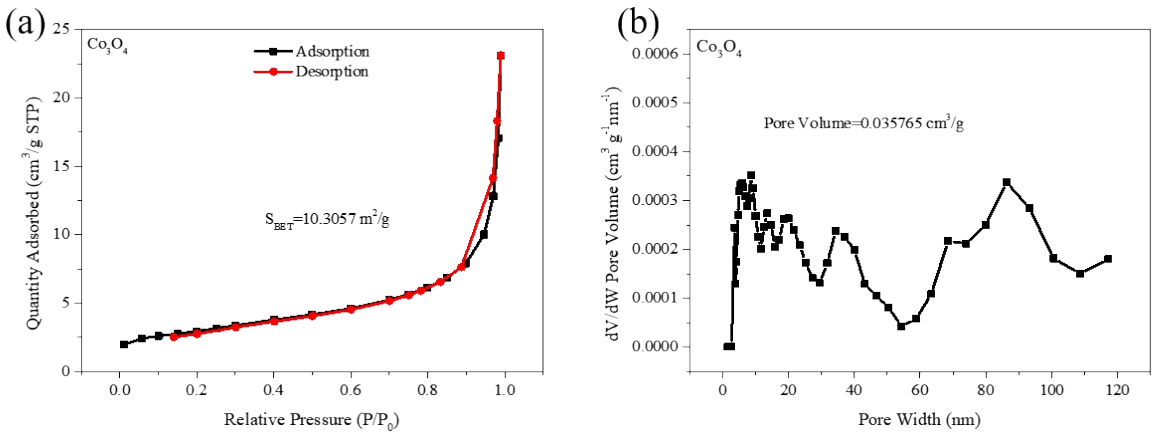

Fig. S6 (a) Nitrogen adsorption-desorption isotherms; (b) pore size distribution of Co_3O_4 catalysts.

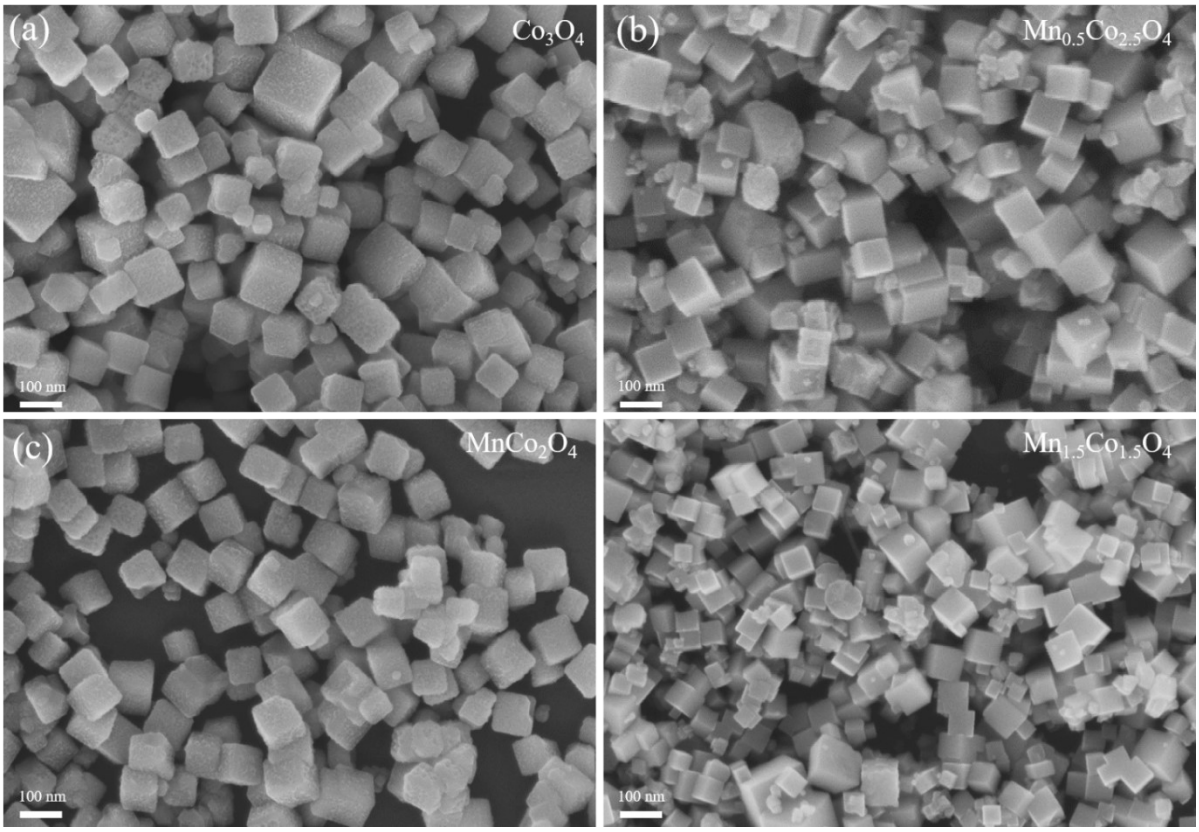

Fig. S7 SEM images of (a) Co_3O_4, (b) $Mn_{0.5}Co_{2.5}O_4$, (c) $MnCo_2O_4$, (d) $Mn_{1.5}Co_{1.5}O_4$ catalysts.

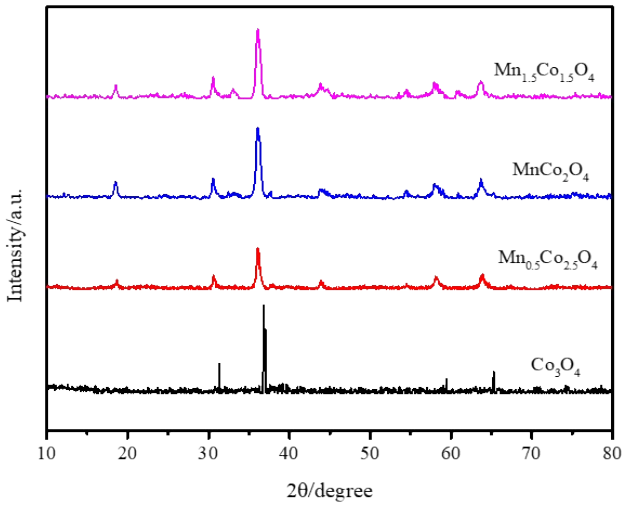

Fig. S8 XRD patterns of Co_3O_4, $Mn_{0.5}Co_{2.5}O_4$, $MnCo_2O_4$, and $Mn_{1.5}$-$Co_{1.5}O_4$ catalysts.

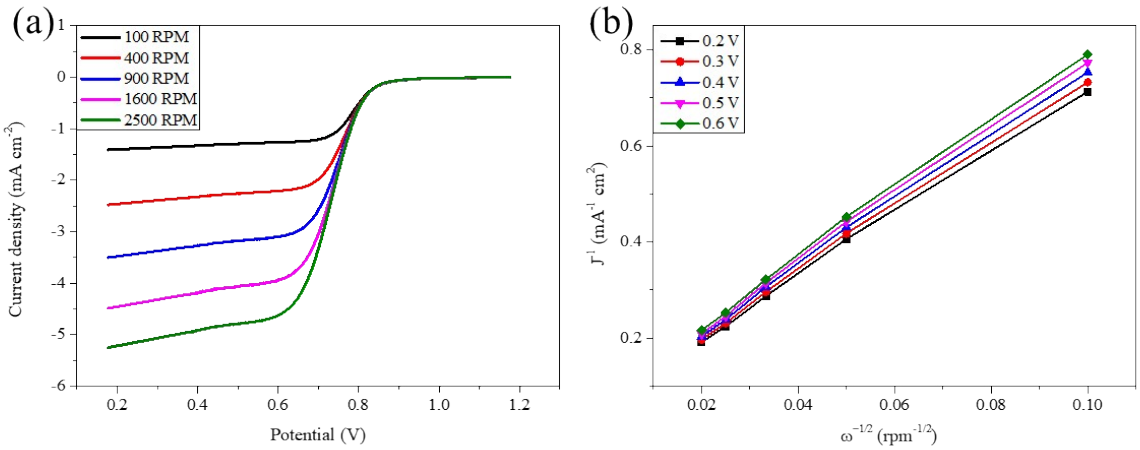

Fig. S9 RDE measure at the different rotation rates and K-L plots of the Co_3O_4.

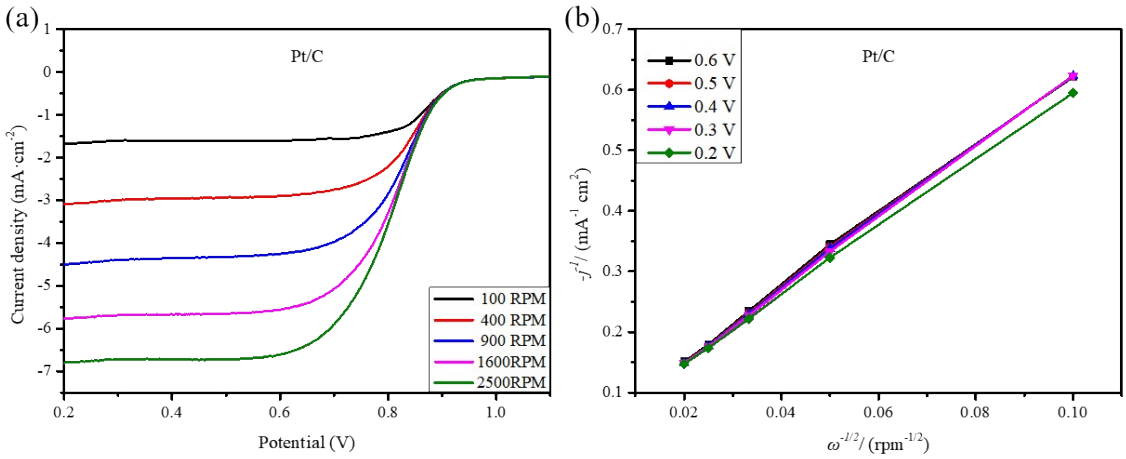

Fig. S10 RDE measure at the different rotation rates and K-L plots of the Pt/C.

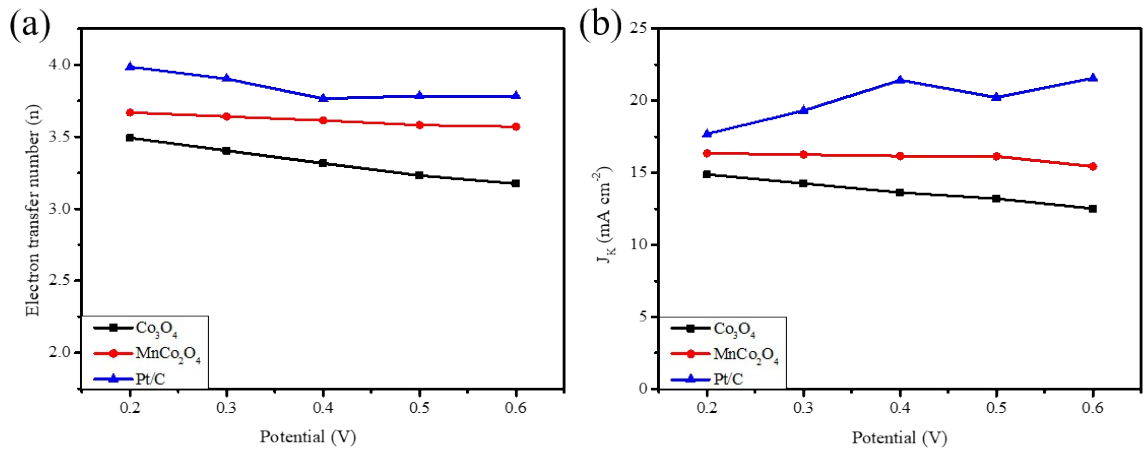

Fig. S11 n and J_K values of the Co_3O_4 and $MnCo_2O_4$.

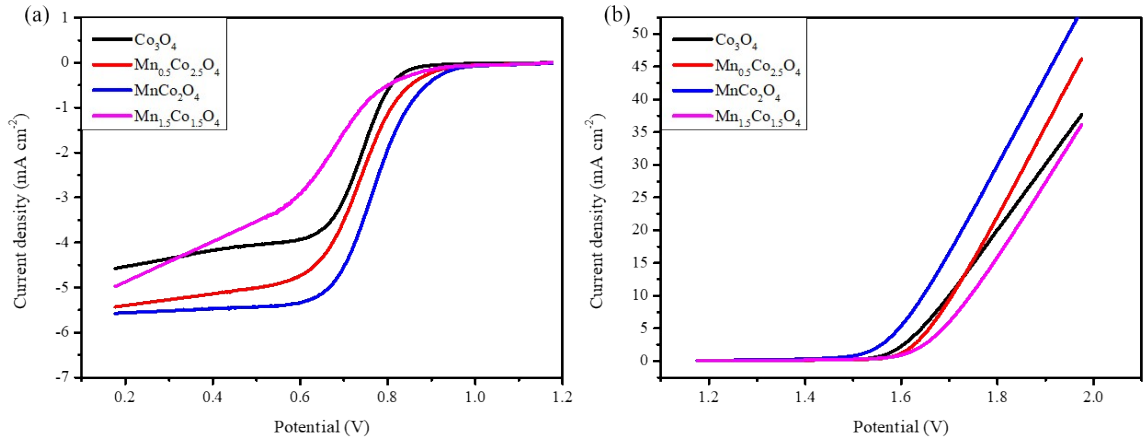

Fig. S12 (a) Oxygen reduction polarization curve and (b) Oxygen evolution polarization curve of Co_3O_4, $Mn_{0.5}Co_{2.5}O_4$, $MnCo_2O_4$, and $Mn_{1.5}Co_{1.5}O_4$ catalysts.

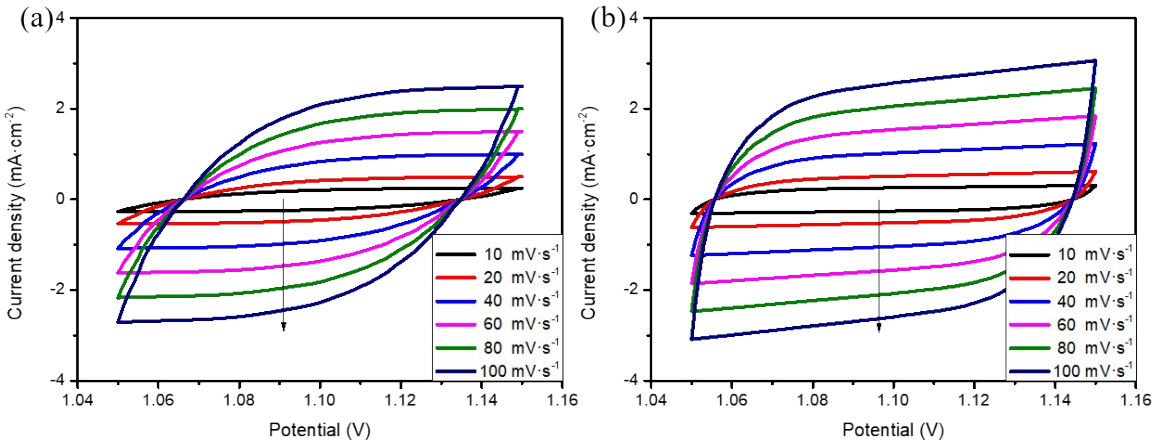

Fig. S13 CV curves at different scan rates of (a) Co_3O_4 and (b) $MnCo_2O_4$.

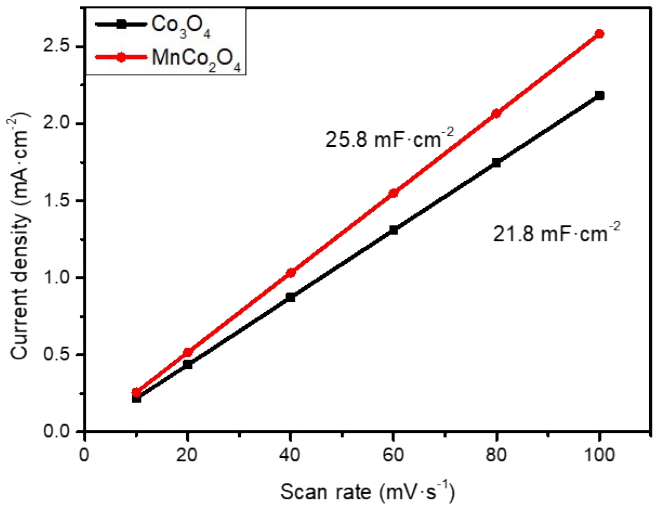

Fig. S14 double-layer capacitance (C_{dl}) values determined by electrochemically active surface area (ECSA) of Co_3O_4 and $MnCo_2O_4$.

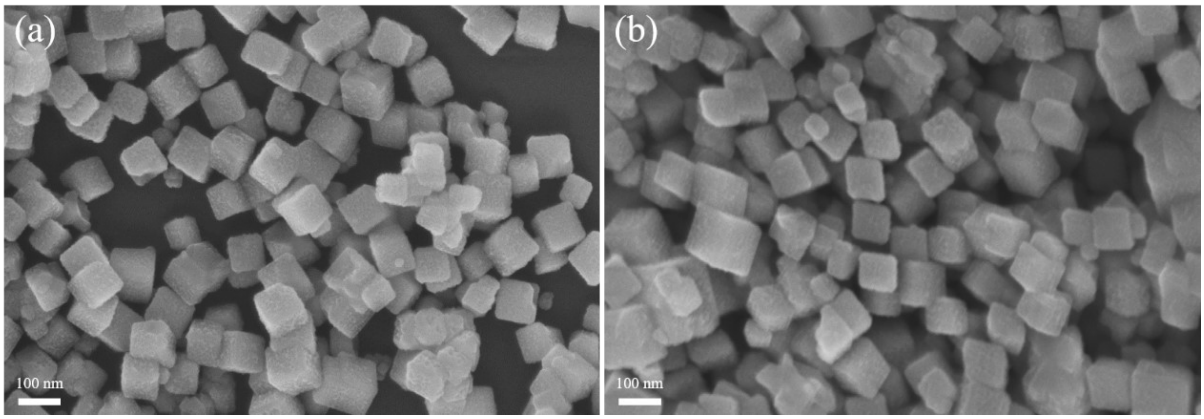

Fig. S15 SEM images of $MnCo_2O_4$ catalyst (a) before and (b) after ORR stability testing.

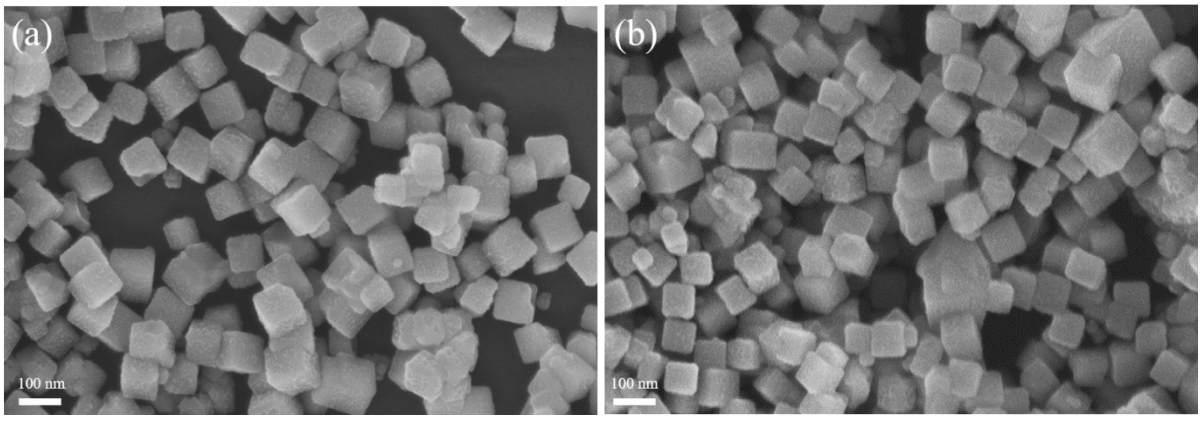

Fig. S16 SEM images of the $MnCo_2O_4$ catalyst (a) before and (b) after OER stability testing.

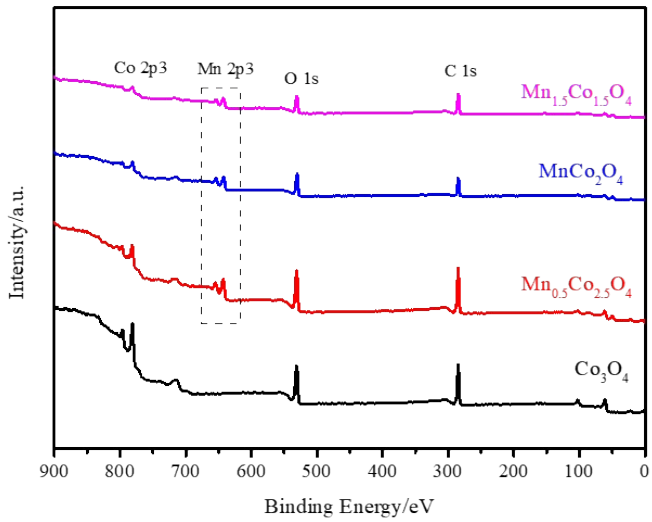

1

2 **Fig. S17** XPS spectra of Co_3O_4, $Mn_{0.5}Co_{2.5}O_4$, $MnCo_2O_4$, and $Mn_{1.5}Co_{1.5}O_4$ catalysts.

3

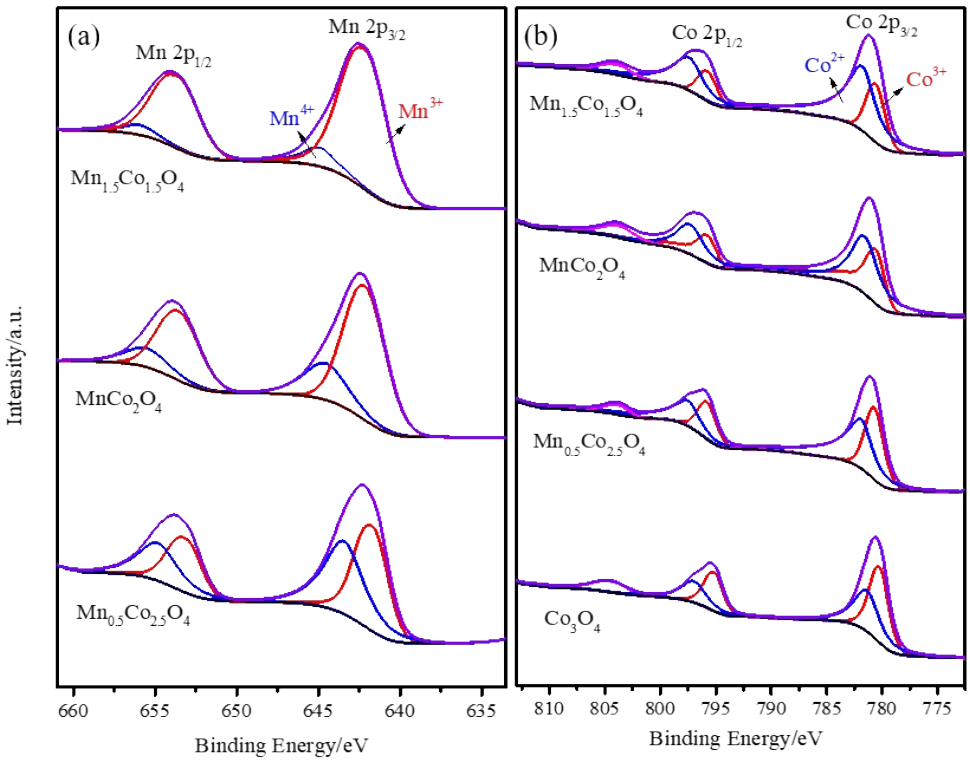

4

5 **Fig. S18** (a) High-resolution Co 2p spectra and (c) High-resolution Mn 2p spectra of Co_3O_4,

6 $Mn_{0.5}Co_{2.5}O_4$, $MnCo_2O_4$, and $Mn_{1.5}Co_{1.5}O_4$ catalysts.

7

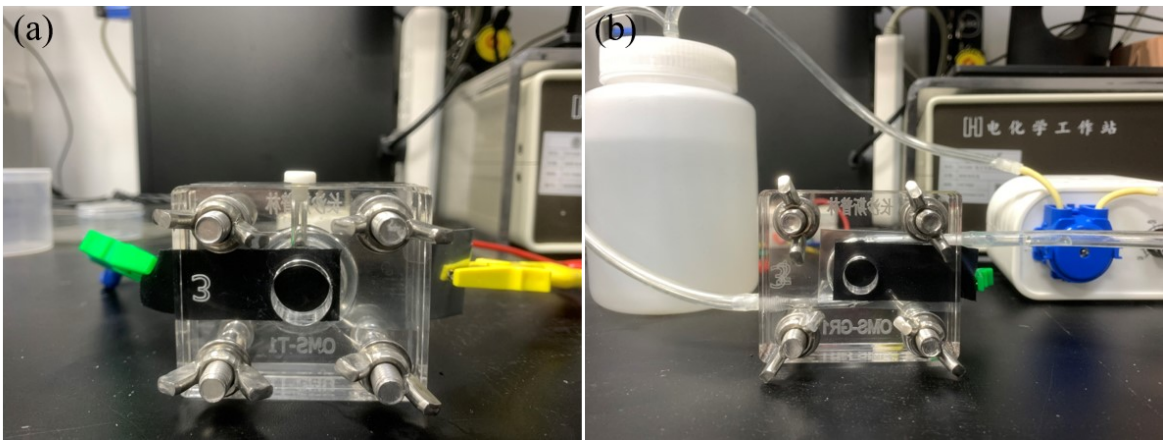

Fig. S19 The photograph of the assembled Zn-air batteries.

Table S1 EDS spectrum results of $MnCo_2O_4$ catalyst.

Spectrum		
Element	***Weight percentage (wt%)***	***Atomic percentage (At%)***
C K	76.58	85.98
O K	13.98	11.79
Mn K	2.96	0.73
Co K	6.48	1.50
Total	100.00	100.00

Table S2 XPS and ICP-OES results of $Mn_XCo_{3-X}O_4$ (X = 0, 0.5, 1, 1.5) catalysts

Samples	Elements	XPS results		ICP-OES results	
		Atomic ratio (%)	Mn/Co	Mass ratio (%)	Mn/Co
Co_3O_4	Mn	0	0	0	0
	Co	8.64		69.65	
$Mn_{0.5}Co_{2.5}O_4$	Mn	1.60	0.203	12.43	0.199
	Co	7.89		65.49	
$MnCo_2O_4$	Mn	3.29	0.491	26.21	0.485
	Co	6.70		56.90	
$Mn_{1.5}Co_{1.5}O_4$	Mn	4.62	0.956	39.04	0.947
	Co	4.83		43.45	

Table S3 ORR onset potential, half-wave potential, limit diffusion current density, Tafel slope, electron transfer number, and kinetic current density of Co_3O_4, $Mn_{0.5}Co_{2.5}O_4$, $MnCo_2O_4$, $Mn_{1.5}Co_{1.5}O_4$ and Pt/C catalysts

Sample	ORR					
	E_{onset} (V)	$E_{1/2}$ (V)	J_L (mA·cm^{-2})	Tafel slope (mV·dec^{-1})	n	J_K (mA·cm^{-2})
Co_3O_4	0.871	0.747	4.16	84.3	3.49	14.89
$Mn_{0.5}Co_{2.5}O_4$	0.947	0.745	5.43	/	/	/
$MnCo_2O_4$	0.976	0.775	5.58	81.6	3.67	16.36
$Mn_{1.5}Co_{1.5}O_4$	0.933	0.667	4.98	/	/	/
Pt/C	0.977	0.849	5.92	59.6	3.98	17.71

Table S4 Potential at 10 mA cm^{-2}, overpotential, Tafel slope, charge transfer resistance and mass activity of Co_3O_4, $Mn_{0.5}Co_{2.5}O_4$, $MnCo_2O_4$, $Mn_{1.5}Co_{1.5}O_4$ and RuO_2 catalysts

Sample	OER				
	$E_{j=10}$ (V)	η (mV)	Tafel slope (mV·dec^{-1})	Rct (Ω)	MA (A·g^{-1})
Co_3O_4	1.70	470	82.6	44.3	34.4
$Mn_{0.5}Co_{2.5}O_4$	1.706	476	/	/	/
$MnCo_2O_4$	1.646	416	62.9	26.14	87.6
$Mn_{1.5}Co_{1.5}O_4$	1.777	547	/	/	/
RuO_2	1.646	416	108.6	/	87.8

Table S5 Cobalt, manganese and oxygen content obtained from XPS of Co_3O_4, $Mn_{0.5}Co_{2.5}O_4$, $MnCo_2O_4$, and $Mn_{1.5}Co_{1.5}O_4$ catalysts.

Sample	Surface Content（%）		
	Co^{2+}/Co^{3+}	Mn^{3+}/Mn^{4+}	O_{ads}/O_{latt}
MnO_2	/	1.58	0.51
Co_3O_4	0.90	/	0.49
$Mn_{0.5}Co_{2.5}O_4$	0.95	1.38	/
$MnCo_2O_4$	1.18	1.98	0.68
$Mn_{1.5}Co_{1.5}O_4$	1.15	1.88	/

Table S6 Performance comparison between Mn-Co_2O_4 and other recently reported electrocatalysts.

Sample	ORR			OER			△E	ZAB stablity
	$E_{1/2}$	Tafel slope	Stability	$E_{j=10}$	Tafel slope	Stability		
Mn-Co_2O_4	0.775	81.6	1.14%	1.646	62.9	1.55%	0.871	70
Co_3O_4	0.747	84.3	8%	1.70	82.6	2.82%	0.953	
Pt/C	0.849	59.6		1.99	201.5		1.141	
RuO_2	0.6	100.3		1.646	63.5		1.046	
α-MnO_2-H_2[10]	0.73	84.6	5%	1.742	199.6	40%	1.012	
RuO_2-carbon nanofiber arrays[11]	0.75			1.65			0.9	33.3
$La_{1.5}Sr_{0.5}NiMn_{0.5}Ru_{0.5}O_6$[12]	0.73			1.66			0.93	
$NiFe_2O_4$-$FeNi_2S_4$[13]	0.507			1.659			1.152	125
ZNCO-NCNTs[14]	0.78	78		1.64	118.3		0.86	33.3
Co_3O_4-LSC[15]	0.69	54		1.61	75		0.92	
NDC-800[16]	0.85	79.53	3.38%	1.63	170.28		0.80	50
Co/Co_9S_8/rGO/MWCNT-800[17]	0.75	72	1.8%	1.68	166		0.89	

References

1. P. C. Hohenberg, W. Kohn, Inhomogeneous Electron Gas, *Phys. Rev.,* 1964, **136**, B864.
2. G. Kresse, J. Furthmüller, Efficient Iterative Schemes for Ab Initio Total-Energy Calculations Using a Plane-Wave Basis Set, *Phys. Rev. B, Condens. Matter,* 1996, **54**, 11169.
3. J. P. Perdew, K. Burke, M. Ernzerhof, Generalized Gradient Approximation Made Simple, *Phys. Rev. Lett.,* 1996, **77**, 3865-3868.
4. G. Kresse, J. Furthmüller, Efficiency of ab-initio total energy calculations for metals and semiconductors using a plane-wave basis set, *Comput. Mater. Sci.,* 1996, **6**, 15-50.
5. G. Kresse, D. Joubert, From ultrasoft pseudopotentials to the projector augmented-wave method, *Phys. Rev. B,* 1999, **59**, 1758-1775.
6. L. Wang, T. Maxisch, G. Ceder, Oxidation energies of transition metal oxides within the GGA+U framework, *Phys. Rev. B, Condens. Matter,* 2006, **73**, 195107.
7. M. T. Curnan, J. R. Kitchin, Effects of Concentration, Crystal Structure, Magnetism, and Electronic Structure Method on First-Principles Oxygen Vacancy Formation Energy Trends in Perovskites, *J. Phys. Chem. C,* 2014, **18**, 28776-28790.
8. V. Viswanathan, H. A. Hansen, J. Rossmeisl, J. K. Nørskov, Universality in Oxygen Reduction Electrocatalysis on Metal Surfaces, *ACS Catal.* 2012, **2**, 1654-1660.
9. I. C. Man, H.-Y. Su, F. Calle-Vallejo, H. A. Hansen, J. I. Martínez, N. G. Inoglu, J. Kitchin, T. F. Jaramillo, J. K. Nørskov, J. Rossmeisl, Universality in Oxygen Evolution Electrocatalysis on Oxide Surfaces, *ChemCatChem,* 2011, **3**, 1159-1165.
10. Q. Zhuang, N. Ma, Z. Yin, X. Yang, Z. Yin, J. Gao, Y. Xu, Z. Gao, H. Wang, J. Kang, D. Xiao, J. Li, X. Li, D. Ma, Rich Surface Oxygen Vacancies of MnO_2 for Enhancing Electrocatalytic Oxygen Reduction and Oxygen Evolution Reactions, *Adv. Energy Sustain. Res.,* 2021, **2**, 2100030.
11. Z. Guo, C. Li, W. Li, H. Guo, X. Su, P. He, Y. Wang, Y. Xia, Ruthenium oxide coated ordered mesoporous carbon nanofiber arrays: a highly bifunctional oxygen electrocatalyst for rechargeable Zn–air batteries, *J. Mater. Chem. A,* 2016, **4**, 6282-6289.
12. M. Retuerto, F. Calle-Vallejo, L. Pascual, G. Lumbeeck, M. T. Fernandez-Diaz, M. Croft, J. Gopalakrishnan, M. A. Peña, J. Hadermann, M. Greenblatt, S. Rojas, $La_{1.5}Sr_{0.5}NiMn_{0.5}Ru_{0.5}O_6$ Double Perovskite with Enhanced ORR/OER Bifunctional Catalytic Activity, *ACS Appl. Mater. Interfaces,* 2019, **11**, 21454-21464.
13. L. An, Z. Zhang, J. Feng, F. Lv, Y. Li, R. Wang, M. Lu, R. B. Gupta, P. Xi, S. Zhang, Heterostructure-Promoted Oxygen Electrocatalysis Enables Rechargeable Zinc–Air Battery with Neutral Aqueous Electrolyte, *J. Am. Chem. Soc.,* 2018, **140**, 17624-17631.
14. X.-T. Wang, T. Ouyang, L. Wang, J.-H. Zhong, Z.-Q. Liu, Surface Reorganization on Electrochemically-Induced Zn–Ni–Co Spinel Oxides for Enhanced Oxygen Electrocatalysis, *Angew. Chem. Int. Ed.,* 2020, **59**, 6492-6499.
15. X. Wang, Z. Pan, X. Chu, K. Huang, Y. Cong, R. Cao, R. Sarangi, L. Li, G. Li, S. Feng, Atomic-Scale Insights into Surface Lattice Oxygen Activation at the Spinel/Perovskite interface of $Co_3O_4/La_{0.3}Sr_{0.7}CoO_3$, *Angew. Chem. Int. Ed.,* 2019, **58**, 11720-11725.
16. P. Li, J. Wen, Y. Xiang, M. Li, Y. Zhao, S. Wang, J. Dou, Y. Li, H. Ma, L. Xu, Hierarchical mesoporous N-doped carbon as an efficient ORR/OER bifunctional electrocatalyst for rechargeable zinc–air battery, *Inorg. Chem. Front.,* 2024, **11**, 5345-5358.
17. Z.-D. Wang, C.-K. Bai, X.-Y. Chen, B.-D. Wang, G.-L. Lu, H. Sun, Z.-N. Liu, H. Huang, S. Liang, H.-Y. Zang, Co/Co_9S_8 nanoparticles coupled with N,S-doped graphene-based mixed-dimensional heterostructures as bifunctional electrocatalysts for the overall oxygen electrode, *Inorg. Chem. Front.,* 2019, **6**, 2558-2565.